Making it big : how characean algae use cytoplasmic streaming to enhance transport in giant cells

Meent, J.W. van de

Citation

Meent, J. W. van de. (2010, September 16). *Making it big : how characean algae use cytoplasmic streaming to enhance transport in giant cells*. *Casimir PhD Series*. Retrieved from https://hdl.handle.net/1887/15949

3 HYDRODYNAMICS OF CYTOPLASMIC STREAMING

Given the complexity and energetic cost of of having a streaming system, it seems clear that cyclosis must confer some significant benefit to the organism. In the last chapter we have seen that streaming is indeed implicated in variety of processes. The most obvious of these is perhaps intercellular transport. Since Charales exhibit growth at the tip, yet are able to take up nutrients and perform photosynthesis all along their surface, there is a clear utility to the transportation of nutrients and cellular building blocks up along the organism. Additionally, streaming may facilitate the formation of alkaline bands, which in turn appears to enhance carbon uptake. These aspects certainly merit further investigation, but in order to narrow down the scope of the current project, we will begin with a closer examination of the hydrodynamics of the internodal flow and their relation to intracellular mixing.

The main aspect that we will focus on in this work, is the question how streaming could help overcome the disadvantages associated with having cells of such a large size. As discussed previously, the notion has often been expressed in the literature that streaming somehow enhances mixing, thereby aiding *homeostasis*, the stabilisation of metabolic rates over fluctuating levels of uptake and demand. Yet few mechanisms have been put forward whose benefits can be quantified. It is our goal to examine the fluid mechanics of this circulation with the hope of elucidating in what way it may contribute to enhancing metabolic rates.

In searching for quantitative descriptions of the benefits of streaming, the characean algae present something of a unique case. The flow in these organisms is perhaps the most organised and symmetrical of all the streaming types found in nature. Two distinguishing features of the Charales that require particular explanation are:

1. The reason for the high streaming rates found *in vivo*, which could presumably only have evolved as a result of considerable genetic pressure.

2. The reason for having a helically directed shear flow that extends into the vacuole.

As discussed in the previous chapter, it is not immediately obvious in what way streaming could enhance mixing within the layer of cytoplasm at the cellular periphery. However exchange between the cytoplasm and vacuole could well be diffusion-limited. Since the vacuole is presumed to help stabilise cytoplasmic concentrations by acting as a buffering reservoir, the mixing of vacuolar contents would be a mechanism for aiding homeostasis as proposed by (Hochachka, 1999).

In this chapter we will analyse the fluid mechanics of the vacuolar flow. Looking at the symmetry of the problem, we find that the helicity of the streaming bands could be relevant to the ability of streaming to aid vacuolar mixing. A system with helical symmetry is found to differ subtly from the simpler axial case with simple straight bands, in that it allows for transverse components absent in the axial flow. A full solution of the flow field shows that these transverse components take the form of a small circulation between the two neutral lines. The magnitude of this circulation depends on the helical pitch of the cell. As we will show in chapter 4, this circulation results in an advection of material from the centre of the vacuole towards the periphery and could thereby be a mechanism for enhancing exchange between vacuole and cytoplasm.

3.1 The Significance of Symmetry in Intracellular Transport

The unique level of symmetry in the geometry of characean internodes makes the system suitable to a relatively straightforward hydrodynamic description. The cytoplasmic bands effectively impose a value for the velocity at the boundaries, so the flow can be modelled as a shear flow inside a cylinder. In this section we'll outline the flow problem to be solved, and explain how the symmetry of the geometry affects the form of the solution.

3.1.1 Stokes Flow Inside a Cylinder

As discussed in the first chapter, the motion of fluids is described by a set of so-called *continuum* equations that govern the time evolution of the density of mass, momentum and energy. Together these equations are known as the *Navier Stokes Equations*, though the term can also refer to the momentum equation alone. In a lot of cases it is not necessary to describe heat flow, so the fluid can effectively be be described by the momentum and mass equations alone. Regular liquids have two basic properties. (1) They are *incompressible*, i.e. their density is constant to good approximation. (2) They are *Newtonian*, i.e. the stress required to shear them is proportional to the rate of strain. For these types of fluids, the equations for momentum and mass are given by (Batchelor, 1967):

$$\rho\left(\frac{\partial \boldsymbol{v}}{\partial t} + \boldsymbol{v}\cdot\nabla\boldsymbol{v}\right) = -\nabla p + \eta\nabla^2\boldsymbol{v}\,, \tag{3.1}$$

$$\rho(\nabla\cdot\boldsymbol{v}) = 0\,. \tag{3.2}$$

Here $\boldsymbol{v}$ is the velocity field, ρ is the density and η is the viscosity of the fluid. The topmost equation (3.1) expresses the evolution of the momentum density. The mass equation (3.2) is also sometimes called the *continuity equation* in this context. For an incompressible fluid, which by definition has a constant density, this equation reduces to the requirement that the flow field has a zero divergence everywhere.

As discussed in chapter 1, it is often convenient to write these types of problems their *dimensionless* form. By specifying a typical length scale and rate of flow, we can renormalize the quantities in these equations as:

$$\boldsymbol{r} = R\tilde{\boldsymbol{r}}\,, \qquad \boldsymbol{v} = V\tilde{\boldsymbol{v}}\,, \qquad t = \frac{R}{V}\tilde{t}\,, \qquad p = \frac{\eta V}{R}\tilde{p} \tag{3.3}$$

After this substitution, the momentum equation takes the form

$$\mathrm{Re}\left(\frac{\partial\tilde{\boldsymbol{v}}}{\partial\tilde{t}} + \tilde{\boldsymbol{v}}\cdot\tilde{\nabla}\tilde{\boldsymbol{v}}\right) = -\tilde{\nabla}\tilde{p} + \tilde{\nabla}^2\tilde{\boldsymbol{v}}\,, \qquad \mathrm{Re} = \frac{\rho V R}{\eta}\,. \tag{3.4}$$

In our case, the typical flow rate V is at most 100 μm/s, whereas the radius of the cell R is at most 500 μm/s. The kinematic viscosity of water $\nu = \eta/\rho$ is equal to 10^{-6} m^2/s. So the Reynolds number is at most 0.05, which means that flow problem can be simplified, by neglecting the leftmost term in (3.1). In this regime, known as *Stokes Flow*, the hydrodynamic equations reduce to:

$$-\nabla p + \nabla^2\boldsymbol{u} = 0\,, \qquad \nabla\cdot\boldsymbol{u} = 0\,. \tag{3.5}$$

Here we have dropped the $\tilde{\boldsymbol{v}}$ notation for convenience. Instead we will use $\boldsymbol{u} = \tilde{\boldsymbol{v}}$ to imply that an equation is in its dimensionless form and $\boldsymbol{v}$ whenever dealing with real units.

It is not immediately clear how we should describe the flow near the endpoints. However, the internodal cells have a very large aspect ratio that typically lies upwards of 30. So for positions sufficiently far away from the endpoints, the flow is well approximated as that inside an infinite cylinder. This assumption is supported by the work by Pickard (1974) on ligated cells, which indicates that the rate of flow is roughly independent of cell length for cells with an aspect ratio $L/R > 5$.

3.1.2 Pickard's Solution for a Cell With Straight Bands

With this simplification in place, we are in a position to examine the simplest version of this flow problem: the case of two straight, non-helical bands flowing along the z-axis. This problem, first solved by by Pickard (1972), reduces to finding the shear flow inside a cylinder under the assumption of two moving bands imposing opposite velocities at the periphery. Because the bands are axially symmetric, the flow is purely directed along the z-axis. It also has a symmetry along this axis if we treat the problem as an infinite cylinder. Likewise, the pressure is symmetric along z in the absence of externally applied gradients. This implies that $\boldsymbol{u}$ and p take the form:

$$\boldsymbol{u} = u_z(r,\theta)\boldsymbol{e}_z \qquad\qquad p = p(r,\theta)\ . \tag{3.6}$$

The continuity equation now reduces to $\partial_z u_z = 0$, which is a condition that is automatically satisfied by symmetry. The three components of the momentum equation become [1] :

$$-\partial_r p = 0\ , \qquad -\frac{1}{r}\partial_\theta p = 0\ , \qquad \nabla^2 u_z = 0\ , \tag{3.7}$$

The first two equations implying that p is simply a constant. The momentum equation therefore reduces to to finding a solution to the problem $\nabla^2 u_z(r,\theta) = 0$, which is just Laplace's equation with Dirichlet boundary conditions – a well-known PDE problem. The solution is readily found by separation of variables:

$$u_z(r,\theta) = \sum_n D^n r^n \sin n\theta\ . \tag{3.8}$$

The application of a step-function boundary condition for the velocity, such that $u_z = 1$ on the upward moving band and $u_z = -1$ on the downward one, then yields coefficients:

$$D^n = \begin{cases} 4/(\pi n) & n \text{ odd} \\ 0 & n \text{ even} \end{cases} \tag{3.9}$$

---

[1] Please note that here is a slight ambiguity in our notation here: $\nabla^2\boldsymbol{u}$ is used to refer to the *vector* Laplacian, whereas $\nabla^2 u_z$ is the *scalar* Laplacian. However, in cylindrical coordinates the z-component of the vector Laplacian is in fact equal to the scalar Laplacian, so there is no need to differentiate between the two in this particular case.

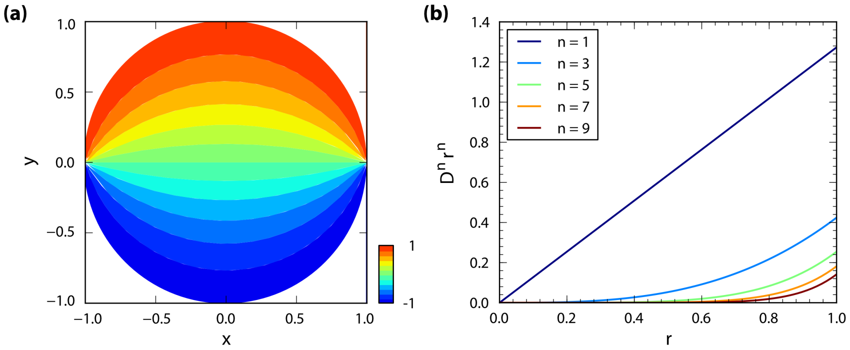

Figure 3.1 The solution in equation 3.10 as obtained by Pickard (1972). **(a)** Contour plot of u_z along the xy-plane. Colours denote the streaming rate along the z-axis. **(b)** Radial modes $D^n r^n$ for $n = 1, 3, 5, 7, 9$.

Pickard (1972) further showed that the series in equation 3.8 converges to a simple analytical form.

$$u_z(r, \theta) = \frac{2}{\pi} \arctan \frac{2r \sin \theta}{1 - r^2} . \qquad (3.10)$$

This form can be seen in figure 3.1, which shows a contour plot of u_z in the xy plane, along with the radial modes $D^n r^n$.

3.1.3 The Péclet Number and the Role of Symmetry

The effect of this advective flow on diffusive dynamics is governed by the *advection-diffusion* equations, that describe the diffusion of a metabolite ρ with diffusion constant D in the presence of a flow field $\boldsymbol{v}$:

$$\partial_t \rho + (\boldsymbol{v} \cdot \nabla)\rho = D\nabla^2 \rho. \qquad (3.11)$$

The relative strength of the advective and diffusive terms is given by the Péclet number, which parametrises the dimensionless form of the equation (see 1.2):

$$\partial_t \rho + \mathrm{Pe}(\boldsymbol{u} \cdot \nabla)\rho = \nabla^2 \rho, \qquad \mathrm{Pe} = VR/D. \qquad (3.12)$$

Again, we employ the convention here that $\boldsymbol{u}$ is taken signify that the velocity and coordinates are now in dimensionless form. The Péclet number contains a typical velocity, a typical length and the diffusion constant of the problem. For V and R we can take the same flow rate of 50 μm/s and the cell radius of 500 μm. Diffusion constants in water range from $D_m \sim 1000$ $\mu m^2/s$ for a small molecule (Nelson, 2004), to $D_p \sim 10$ $\mu m^2/s$ for larger proteins (Phillips et al., 2008). Péclet numbers will therefore lie somewhere in the range of 25-2500, depending on the type of solute, and flows are therefore moderately to strongly advection-dominated.

However in spite of these high Péclet numbers, the effect of streaming on transport will still depend qualitatively on the symmetry of the problem. In the case of the approximate solution by Pickard for example, the flow field only has a z-component, and therefore only couples to gradients along the z-axis. Hence there is no mechanism for enhancement of radial transport. Of course, even an axially symmetric flow can be subject to effects like Taylor Dispersion, whereby spreading along the direction of flow is enhanced since diffusing molecules will spend varying amounts of time in regions of high flow (Taylor, 1953, 1954a,b). However, these effects only become dominant over transport distances $\Delta z/R \gg \mathrm{Pe}$ where enough diffusion along the radial direction takes place to result in a dispersion of advection rates. In the case of this system this would mean that Taylor Diffusion would only become significant on time scales equivalent to multiple loops up and down the cell.

So while Péclet numbers can be nominally large, it is not immediately clear how streaming would serve to enhance vacuolar mixing in the case of straight bands. The symmetry of the helical case is subtly different in this respect. This difference is rooted in the fact that the chiral symmetry is broken in this system, since a spiral can be either left- or right-handed. So whereas the axial case is invariant under left-right reversal along the x-axis, the helical case is not. This implies that there could in principle exist a left-right asymmetry in the resulting flow field that allows for radial advection. This radial advection in turn could aid vacuolar mixing in a way that is qualitatively absent in the axial case.

To investigate this idea further, we will write down a full solution of the helical problem. Before we do so, however, we will examine the symmetry properties of the helical case to see in what way this change in symmetry affects the flow field.

3.1.4 Helical Symmetry in the Characean Internode

The basic property of a system with helical symmetry is that there is an invariance under a combined translation and proportional rotation.

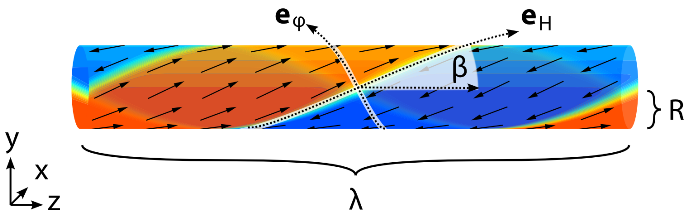

Figure 3.2 Helical coordinate system and boundary conditions used in solution of streaming flow. Shown are the downstream axis $\boldsymbol{e}_H$, oriented parallel to the streaming bands, and the spanwise axis $\boldsymbol{e}_\varphi$, oriented perpendicular to the bands.

Figure 3.2 shows the case of an internodal cell approximated as an infinite cylinder. The flow field here is symmetric, in the sense that it is invariant along the z-axis up to a rotation κz. The single parameter of this symmetry is the wave number κ which specifies a rate of rotation periodic over the wavelength $\lambda = 2\pi/\kappa$ of the bands. In the literature, the pitch of the helix is also sometimes measured by the angle β that the neutral line makes with respect to the z-axis, which can be related to κ by $\beta = \arctan(\kappa R) = \arctan(2\pi R/\lambda)$.

A natural coordinate with respect to this invariance is the helical angle $\varphi = \theta - \kappa z$, which is just the cylindrical angle θ corrected for the helical orientation κz. Now by definition, any solution of the flow field may only depend on the r and φ coordinates, since the system is invariant under all transformations that preserve φ.

A corollary of this choice of coordinates is that it also determines a corresponding set of basis vectors. Keeping the radial coordinate and its basis vector, the basis vector $\boldsymbol{e}_\varphi = \nabla\varphi/|\nabla\varphi|$ can be uniquely obtained from the gradient of the coordinate, and a third axis $\boldsymbol{e}_H = \boldsymbol{e}_r \times \boldsymbol{e}_\varphi$ is now determined by orthogonality with respect to the other two. The basis transformation then takes the following form:

$$\boldsymbol{e}_r = \boldsymbol{e}_r\,, \quad \boldsymbol{e}_\varphi = \frac{1}{h}(\boldsymbol{e}_\theta - \kappa r \boldsymbol{e}_z)\,, \quad \boldsymbol{e}_H = \frac{1}{h}(\kappa r \boldsymbol{e}_\theta + \boldsymbol{e}_z)\,, \tag{3.13}$$

where $h = \sqrt{1+\kappa^2 r^2}$. The reverse transformation is given by:

$$\boldsymbol{e}_r = \boldsymbol{e}_r\,, \quad \boldsymbol{e}_\theta = \frac{1}{h}(\boldsymbol{e}_\varphi + \kappa r \boldsymbol{e}_H)\,, \quad \boldsymbol{e}_z = \frac{1}{h}(\kappa r \boldsymbol{e}_\theta - \boldsymbol{e}_H)\,. \tag{3.14}$$

As illustrated in figure 3.2, the vector $\boldsymbol{e}_H$ is aligned parallel to the bands everywhere, and thus points along the axis of symmetry. The vector $\boldsymbol{e}_\varphi$ is orthogonal to the bands at every point.

It should be noted that while the choice of φ uniquely specifies the basis vectors, it does not determine a unique coordinate H along the helical axis. In fact, a peculiarity of helical coordinate systems is that there is no global coordinate function H such that $\nabla H / |\nabla H| = \boldsymbol{e}_H$. [2] While this would be problematic in a non-symmetric system, we can gloss over this problem in our case, since the symmetry dictates that there is no H-dependence anyway.

The lack of unique global coordinate leaves a degree of freedom in our choice of the metric for the coordinate system, which defines the local coordinate dependence. While this choice leaves the basis set unchanged, it does affect the form of differential operators. One of the more convenient choices turns out to be to enforce the constraint $\Delta\varphi\Delta H \propto r$. Hereby a surface of constant r, and area $r\Delta\theta\Delta z$, maps to a fixed interval in φ and H for all r. The real space distance of an infinitesimal displacement in terms of the change in coordinates is given by the *line element* of the metric. With our current choice of coordinates this line element then becomes:

$$ds^2 = dr^2 + \frac{r^2}{h^2} d\varphi^2 + h^2 dH^2 \, . \tag{3.15}$$

Given this metric, the gradient takes the following form:

$$\nabla f = \frac{\partial f}{\partial r}\boldsymbol{e}_r + \frac{h}{r}\frac{\partial f}{\partial \varphi}\boldsymbol{e}_\varphi + \frac{1}{h}\frac{\partial f}{\partial H}\boldsymbol{e}_H \, . \tag{3.16}$$

The divergence takes the form

$$\nabla \cdot \boldsymbol{v} = \frac{1}{r}\frac{\partial}{\partial r}(r v_r) + \frac{h}{r}\frac{\partial v_\varphi}{\partial \varphi} + \frac{\partial v_H}{\partial H} \, , \tag{3.17}$$

---

[2] To see this, imagine following the line pointing along $\boldsymbol{e}_\varphi$ in figure 3.2. If you start at one of the neutral lines and keep going for an entire period in φ, you end up on the same neutral line where you started, but at a different point along the band. However, this point should have the same H coordinate, since you only moved along φ. The only way this could be true was if H were a periodic coordinate like φ, but then H could never be used to span the surface area of an infinite cylinder. So a global coordinate for H simply does not exist.

and the curl can be written as

$$\begin{aligned}
\nabla \times \boldsymbol{v} = {} & \left[\frac{1}{r}\frac{\partial v_H}{\partial \varphi} - \frac{1}{h}\frac{\partial v_\varphi}{\partial H}\right]\boldsymbol{e}_r \\
& + \left[\frac{1}{h}\frac{\partial v_r}{\partial H} - \frac{1}{h}\frac{\partial}{\partial r}(h v_H)\right]\boldsymbol{e}_\varphi \\
& + \left[\frac{h}{r}\frac{\partial}{\partial r}\left(\frac{r}{h}v_\varphi\right) - \frac{h}{r}\frac{\partial v_r}{\partial f}\right] e_H \, .
\end{aligned} \tag{3.18}$$

The vector Laplacian, which is in general defined by $\nabla^2 \boldsymbol{v} = \nabla(\nabla \cdot \boldsymbol{v}) - \nabla \times (\nabla \times \boldsymbol{v})$, takes the form:

$$\begin{aligned}
\nabla^2 \boldsymbol{v} = {} & \left[\frac{\partial}{\partial r}\left(\frac{1}{r}\frac{\partial}{\partial r}(r v_r)\right) + \frac{h^2}{r^2}\frac{\partial^2 v_r}{\partial \varphi^2} + \frac{1}{h^2}\frac{\partial^2 v_r}{\partial H^2}\right. \\
& \qquad \left. - \frac{2}{r^2 h}\frac{\partial v_\varphi}{\partial \varphi} - \frac{2h'}{h^2}\frac{\partial v_H}{\partial H}\right]\boldsymbol{e}_r \\
& + \left[\frac{\partial}{\partial r}\left(\frac{1}{r}\frac{\partial}{\partial r}(r v_\varphi)\right) + \frac{h'^2}{h^2}v_\varphi + \frac{h^2}{r^2}\frac{\partial^2 v_\varphi}{\partial \varphi^2}\right. \\
& \qquad \left. + \frac{1}{h^2}\frac{\partial^2 v_\varphi}{\partial H^2} + \frac{2}{r^2 h}\frac{\partial v_r}{\partial \varphi}\right]\boldsymbol{e}_\varphi \\
& + \left[\frac{\partial}{\partial r}\left(\frac{1}{r}\frac{\partial}{\partial r}(r v_H)\right) + \frac{1 + 4\kappa^2 r^2}{r^2 h^4}v_H + \frac{h^2}{r^2}\frac{\partial^2 v_H}{\partial \varphi^2}\right. \\
& \qquad \left. + \frac{1}{h^2}\frac{\partial^2 v_H}{\partial H^2} + \frac{2h'}{h^2}\frac{\partial v_r}{\partial H}\right]\boldsymbol{e}_H
\end{aligned} \tag{3.19}$$

3.1.5 Downstream and Stream function Components of Flow

The above expression for the Laplacian in fact proves rather impractical when solving the Stokes equations (3.5). However, the helical coordinates are very useful in highlighting the symmetry properties of the system. Like in most shear flows, there is a natural separation of the downstream component u_H w.r.t to the two wall-normal and spanwise components u_r and u_φ. Having approximated the system as an infinite cylinder, the flow is invariant along H and the continuity equation simplifies to

$$\nabla \cdot \boldsymbol{u} = \frac{1}{r}\left(\frac{\partial}{\partial r}(r u_r) + h\frac{\partial u_\varphi}{\partial \varphi}\right) = 0 \, . \tag{3.20}$$

The introduction of a so-called *stream function* $\Psi(r, \varphi)$ can now ensure that the continuity condition is satisfied by construction. This stream function is defined through the relation

$$\boldsymbol{u}(r, \varphi) = w(r, \varphi)\mathbf{e}_H - \frac{1}{h}\nabla\Psi(r, \varphi) \times \mathbf{e}_H \, . \tag{3.21}$$

The components u_r and u_φ are therefore given by:

$$u_r = -\frac{1}{r}\frac{\partial\Psi}{\partial\varphi} \, , \qquad u_\varphi = \frac{1}{h}\frac{\partial\Psi}{\partial r} \, , \tag{3.22}$$

and the continuity equation (3.20) is satisfied identically, as:

$$\nabla \cdot \boldsymbol{u} = \frac{1}{r}\left(-\partial_r\partial_\varphi\Psi + \partial_\varphi\partial_r\Psi\right) = 0 \, .$$

A corollary of this decomposition is that streaming will influence diffusion along the downstream and transverse axes in distinctly different ways. Like the flow field, the advective term in advection-diffusion equation (3.12) expands into a downstream and transverse part:

$$(\boldsymbol{u} \cdot \nabla)\rho = w(r, \varphi)\frac{\partial\rho}{\partial H} - \frac{1}{r}\frac{\partial\Psi}{\partial\varphi}\frac{\partial\rho}{\partial r} + \frac{1}{r}\frac{\partial\Psi}{\partial r}\frac{\partial\rho}{\partial\varphi} \, .$$

So whereas the downstream component couples to the gradients along the H-axis, it is the stream function terms that affects transport along the radial and spanwise directions.

In the approximation as presented by Pickard (equation 3.10), which is equivalent to a helical coordinate system in the limit $\lambda \to \infty$, flow is purely directed along the axis of symmetry and no coupling in the radial or spanwise directions takes place. This approximation could be appropriate for intercellular transport problems, where the concentration gradients are predominantly longitudinal.

On the other hand, if boundary conditions are such that the advection-diffusion equations share the symmetry of the flow field, it is the stream function components that determine the effect of advection on diffusive transport. The simplest and most obvious example of this is the case where an outside concentration $\rho_b = \rho_b(t)$ is approximately constant at the surface of the cell and depends only on time. The significance of this is that we should expect precisely *global* changes in concentration, which have no mean variation along the helical axis, to be sensitive to the transverse components of flow.

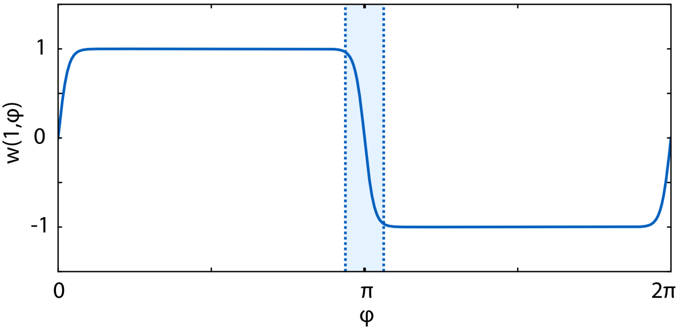

Figure 3.3 Boundary value for the solution $\boldsymbol{u}(1,\varphi) = w(1,\varphi)\boldsymbol{e}_H$. We use a tanh dependence to smooth out the cross-over at the boundaries. This dependence has a characteristic width ε, resulting in a gradient that extends over a neighbourhood of about 4ε around the neutral line. In most of our calculations we use $\varepsilon = \pi/32$, corresponding to a neighbourhood width of about 200 µm. This is larger than the typical widths found in vivo (40 µm) but sufficiently precise for our purposes.

3.2 Solution of the Flow Field

In the previous section we have seen that the symmetry of a helical internode allows for a flow field that is qualitatively different from that of a cell with straight bands. The distinction between the two is that the stream function components of flow are zero in the axial case, whereas in the helical geometry stream function components are not necessarily zero. This difference is ultimately rooted in the broken chiral symmetry of a helical system, which must be either left-handed or right-handed. In this section we proceed to obtain a full solution of the helical flow field to investigate what form these stream function components take and learn how they might aid in redistributing vacuolar content.

As we have seen in the previous section, the hydrodynamical problem at hand is that of obtaining the Stokes flow solution inside an infinite cylinder with a specified velocity at the boundary. Meleshko et al. (2000) have shown that this type of problem can be solved as a Fourier-Bessel expansion in cylindrical coordinates. Given the somewhat unwieldy form of the vector Laplacian in helical coordinates (eq 3.19), this approach indeed proves to be the most practical to our case. We will therefore initially solve for a set of flow components (u_r, u_θ, u_z) and then reconstruct $w(r,\varphi)$ and $\Psi(r,\varphi)$ from the solved forms.

In defining our boundary velocity at $r = R$, we will take a piecewise constant value U over the top and bottom domains $\varphi = [0, \pi)$ and $\varphi = [\pi, 2\pi)$. The direction of flow reverses at the two neutral lines located at $\varphi = 0$ and $\varphi = \pi$. These neutral lines are typically characterised by a single row of missing chloroplasts, so the reversal takes place over a narrow neighbourhood ϵ of order 10 μm. Rather than approximating the boundary velocity with a step-function, which will result in poor convergence of the Fourier expansion due to ringing artefacts, we will keep this finite length ϵ and use a hyperbolic-tangent dependence near the neutral lines to obtain a continuous cross-over (see figure 3.3). The dimensionless form of the downstream component w thus becomes

$$w(1, \varphi) = \begin{cases} \tanh(\varphi/\epsilon) & 0 \le \varphi < \pi/2 \\ -\tanh((\varphi - \pi)/\epsilon) & \pi/2 \le \varphi < 3\pi/2 \\ \tanh((\varphi - 2\pi)/\epsilon) & 3\pi/2 \le \varphi < 2\pi \end{cases} . \qquad (3.23)$$

Following Meleshko et al. (2000), the hydrodynamic solution can now be obtained from the boundary conditions as a mode expansion (Goldstein et al., 2008). The θ and z dependence in the general solution takes the form of a double sum over Fourier modes. Since the boundary velocity is odd around both $\varphi = 0$ and $\varphi = \pi$, its Fourier expansion will have the form

$$\boldsymbol{u}(1, \varphi) = \sum_{n \text{ odd}} W^n \sin(n\varphi) \boldsymbol{e}_H \,, \qquad (3.24)$$

Here W^n are the Fourier expansion coefficients of the boundary condition specified in (3.23). Translation of this form to cylindrical coordinates yields.

$$\begin{aligned} u_\theta(1, \theta, z) &= \frac{\kappa}{\sqrt{1+\kappa^2}} \sum_{n \text{ odd}} W^n \sin(n(\theta - \kappa z)) \,, \\ u_z(1, \theta, z) &= \frac{1}{\sqrt{1+\kappa^2}} \sum_{n \text{ odd}} W^n \sin(n(\theta - \kappa z)) \,. \end{aligned}$$

So we see that the velocity components at the boundary behave as $\sin(n\varphi)$. Because of the linearity of the Stokes equations the same must be true for all r. So whereas the general solution would take the form of a double sum over modes in θ and z, the symmetry of the problem is reflected in the fact that only specific combinations of modes in θ and z contribute. These combinations can be written out explicitly by using that

$$\sin(a + b) = \sin(a)\cos(b) - \cos(b)\sin(a)$$

to expand the relations above to

$$\begin{aligned}
u_\theta^n(r,\theta,z) &= u_\theta^n(r)[\sin(n\theta)\cos(n\kappa z) - \cos(n\theta)\sin(n\kappa z)]\,, \\
u_z^n(r,\theta,z) &= u_z^n(r)[\sin(n\theta)\cos(n\kappa z) - \cos(n\theta)\sin(n\kappa z)]\,.
\end{aligned}$$

The requirement that $\nabla \cdot \boldsymbol{u} = 0$ now determines that u_r should have the form

$$\begin{aligned}
u_r^n(r,\theta,z) &= u_r^n(r)[\cos(n\theta)\cos(n\kappa z) + \sin(n\theta)\sin(n\kappa z)] \\
&= u_r^n(r)\cos(n\varphi)\,.
\end{aligned}$$

Similarly, the pressure will need to take the form $p^n \sim \cos(n\varphi)$ to satisfy the momentum equation $\nabla^2 \boldsymbol{u} = \nabla p$.

So we have found that only combinations of modes that depend on $\varphi = \theta - \kappa z$ contribute to the solution, as is required since our final solution my only depend on (r,φ) coordinates. So the fact that we are solving a problem with two variables instead of three means that the double sum in the general solution reduces to a single sum in our case. The form of the solution we will obtain is therefore:

$$u_r(r,\varphi) = \sum_{n\text{ odd}} u_r^n(r)\cos(n\varphi), \tag{3.25a}$$

$$u_\theta(r,\varphi) = \sum_{n\text{ odd}} u_\theta^n(r)\sin(n\varphi), \tag{3.25b}$$

$$u_z(r,\varphi) = \sum_{n\text{ odd}} u_z^n(r)\sin(n\varphi), \tag{3.25c}$$

$$p(r,\varphi) = \sum_{n\text{ odd}} \eta p^n(r)\cos(n\varphi)\,. \tag{3.25d}$$

To find the radial modes, we now introduce the substitution

$$u_r^n = -(a^n + b^n)/2\,, \qquad u_\theta^n = -(a^n - b^n)\,.$$

These modes can now be substituted into the equations for Stokes flow (3.5). As shown by Meleshko et al. (2000), the solutions for the radial modes then the form of a combination of modified Bessel functions

$$\begin{aligned} a_r^n(r) &= \frac{1}{I_n(n\kappa)}\left[A^n I_{n+1}(n\kappa r) + P^n \frac{\kappa r}{2\pi} I'_{n+1}(n\kappa r)\right], && (3.26a) \\ b_r^n(r) &= \frac{1}{I_n(n\kappa)}\left[B^n I_{n-1}(n\kappa r) + P^n \frac{\kappa r}{2\pi} I'_{n-1}(n\kappa r)\right], && (3.26b) \\ u_z^n(r) &= -\frac{1}{I_n(n\kappa)}\left[C^n I_n(n\kappa r) + P^n \frac{\kappa r}{2\pi} I'_n(n\kappa r)\right], && (3.26c) \\ p_r^n(r) &= -\frac{1}{I_n(n\kappa)}\left[P^n \frac{\kappa}{\pi} I_n(n\kappa r)\right]. && (3.26d) \end{aligned}$$

The form above satisfies the momentum equation. The continuity equation reduces to a simple relation between the coefficients

$$P^n = -n\pi(A^n + B^n - 2C^n)\,. \tag{3.27}$$

This relation allows us to eliminate P^n from equations 3.26(a-c), which after substitution of $r = 1$ reduce to a linear system of equations that can be used to obtain A^n, B^n and C^n from the boundary velocity coefficients W^n. This problem can be readily solved using standard linear algebra software.

The coefficients A^n, B^n and C^n now determine our radial functions $a^n(r)$, $b^n(r)$ and $u_z^n(r)$, which relate to $w^n(r)$, $u_\varphi^n(r)$ and $\Psi^n(r)$ through the relations

$$\begin{aligned} u_\varphi^n(r) &= -\frac{1}{h}(a^n(r) - b^n(r) + \kappa r u_z^n(r))\,, && (3.28a) \\ w^n(r) &= -\frac{1}{h}(-\kappa r a^n(r) + \kappa r b^n(r) + u_z^n(r))\,, && (3.28b) \\ \Psi^n(r) &= -\frac{r}{n} u_r^n(r)\,. && (3.28c) \end{aligned}$$

3.2.1 Properties of the Solved Modes

Having obtained the radial modes through the method above, we are now in a position to examine the effect of helicity on the internodal flow. A series of panels in figure 3.4 shows the downstream component $\boldsymbol{u}_H = w\boldsymbol{e}_H$ and the stream function components $\boldsymbol{u}_\Psi = -(\nabla\Psi)/h \times \boldsymbol{e}_H$ for a series of wavelengths $\lambda = 3.0, 12.0$, and 25.0. The colours denote the projection of each component along the z-axis, with the arrows showing the in-plane projections.

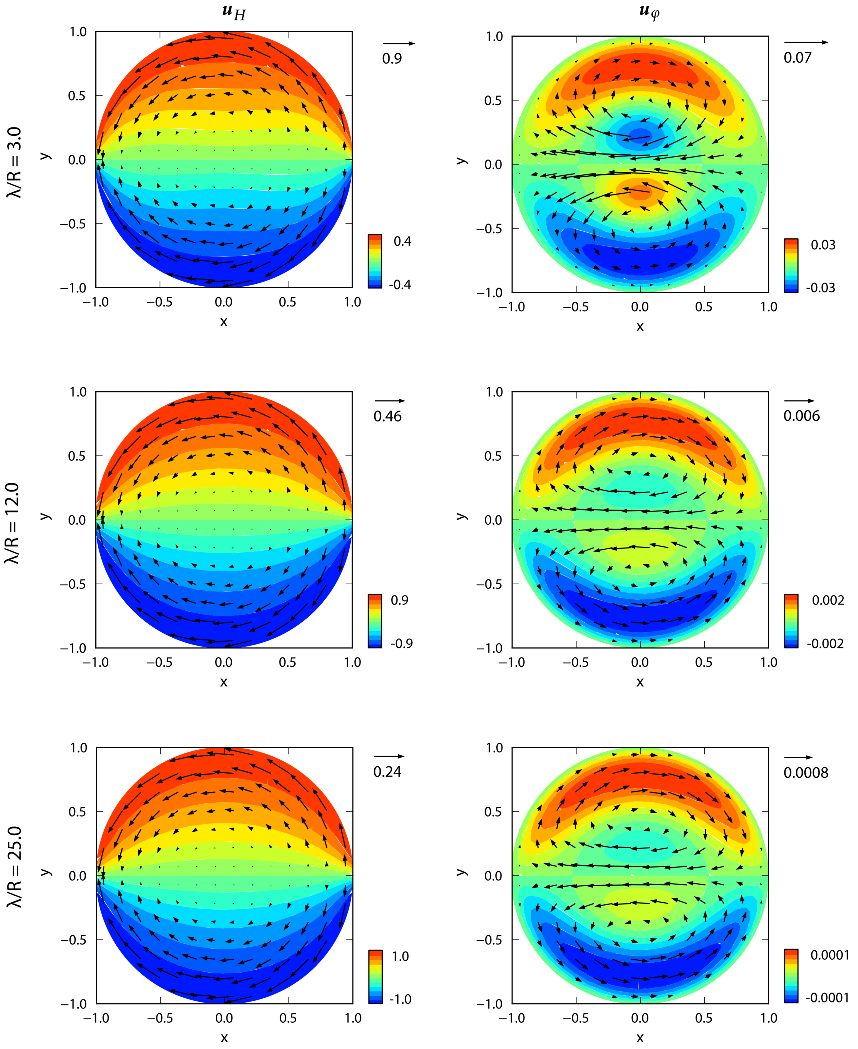

Figure 3.4 Contour plots of helical and stream function components of flow for wavelengths $\lambda = 3.0, 12.0, 25.0$. The colours denote the magnitude along the z-axis, with arrows indicating the magnitude of the in-plane flow. The morphology of the solution shows a weak dependence on the wavelength, and aside from its orientation the helical term is very similar to its asymptotic $\lambda \to \infty$ solution as solved by Pickard (1972) (see figure 3.9). The stream function component shows a double circulation loop through the centre of the cell, the magnitude of which depends strongly on the helical wavelength.

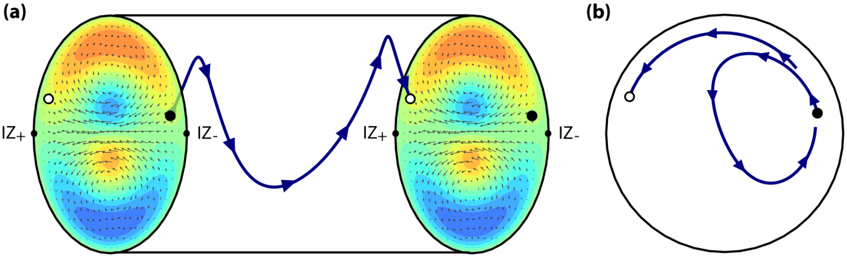

Figure 3.5 Illustration of advective trajectories in a spiralling internodal flow. Shown is the path of a parcel near one of the neutral lines over one helical period, in a flow with λ=3 and ε=π/32. **(a)** Path of a fluid parcel with starting coordinates $r = 0.8$ and $\varphi = \pi/16$. **(b)** Projection of the trajectory onto the xy-plane.

As is to be expected, the downstream component takes a form that is qualitatively similar to the Pickard solution (fig 3.1). The wavelength dependence in this component is weak, in the sense that there are no immediately observable differences in the cross-sectional profiles, aside from a trivial shift in orientation along the helical axis.

The main finding resulting from this analysis is that the helicity of the flow does in fact imply the existence of stream function components of flow. These components take the form of a gentle circulation that moves between the neutral lines, looping back along the inside of the bands. Note that the stream function components approach zero near the boundary, since by definition $\boldsymbol{u}(1,\varphi) = w(1,\varphi)\boldsymbol{e}_H$. The stream function mode is qualitatively similar across different wavelengths, but its magnitude decreases steeply as λ approaches infinity. Taking $\lambda = 12$ as a typical number for the minimum wavelength during cellular development, we see that the magnitude of this flow is a modest 0.5% of the wall-velocity. Yet with wall Péclet numbers that can easily lie upwards of 100, the effects of this small advection could well be significant.

For the purposes of illustrating the effect we show an advective trajectory in figure 3.5. In trajectories of fluid parcels near the neutral lines for example, as shown here for a trajectory with $\lambda = 3$ and $\varepsilon = \pi/32$, we see that a fluid particle can traverse the centre of the cell when it is follwed along the z-direction over a distance equivalent to the wavelength of one helical pitch. Since the circulation along the (r, φ)-coordinates takes place in an advective frame along the H-axis, the real-word trajectories can be nontrivial, producing spiralling forms as shown in panel b. The time scales of these circulation loops will be analysed further in chapter 4.

The scalar fields p and Ψ are shown in figure 3.6. The pressure shows two extrema at the neutral lines, reflecting the same asymmetry related to the handedness of the spiral as is observed in the stream function components. As with the components of flow, the solutions show a great deal of similarity across wavelengths. A slight dependence on the cross-over width manifests itself in that the extrema at $\varphi = 0$ and $\varphi = \pi$ become more confined as ε decreases.

The corresponding Ψ cross sections show two rounded extrema in the upper and lower half plane. The isocontours of these extrema mark the trajectories that particles follow when advected by the transverse components $\boldsymbol{u}_\Psi$. As the cross-over width decreases, a subtle sharpening of the corners of these contours is visible, but the field is qualitatively very similar across different values of both ε and λ.

Given the weak dependence on the cross-over width, we will use $\varepsilon = \pi/32$ for reasons of numerical convenience, unless otherwise stated. For a typical cell, this corresponds to a cross-over width of about $4\varepsilon R = 200$ µm.

Looking at the solved radial modes (figure 3.7), we see that the solutions for $u_H^n(r)$ and $p^n(r)$ are in fact highly similar in shape. However, this similarity is not immediately apparent when examining the equations. Note that the 2-dimensional profiles take a quite different form as a result of the fact that $u_H \sim \sin(n\varphi)$ while $p \sim \cos(n\varphi)$.

The modes for $u_r^n(r)$ and $u_\varphi^n(r)$ show that the stream function components are dominated by the first mode, which determines the rate of circulation at the centre of the cell $u_r^1(0)$. Note that both the stream function modes and their derivatives $\partial_r u_\varphi^n(r)$ approach zero at the boundary, as is required in order for the velocity field to be divergence free. Figure 3.8 shows the modes for the stream function. The extrema in figure 3.4 show up as a single maximum in the first mode, with higher order terms responsible for the subtle changes in corner shape observed for varying ε.

Since the stream function components are all but determined by their first mode constituent term, the following simple form provides a useful approximation for the stream function:

$$\Psi(r, \varphi) \simeq \alpha_\psi r(1 - r^2)^2 \sin(\varphi) . \tag{3.29}$$

The amplitude $\alpha_\psi = -u_r^1(0)$ is equal to the rate of flow through the centre of the cell. The dotted line in figure 3.8 shows the approximation of the first mode. While the polynomial approximation of the first mode is entirely

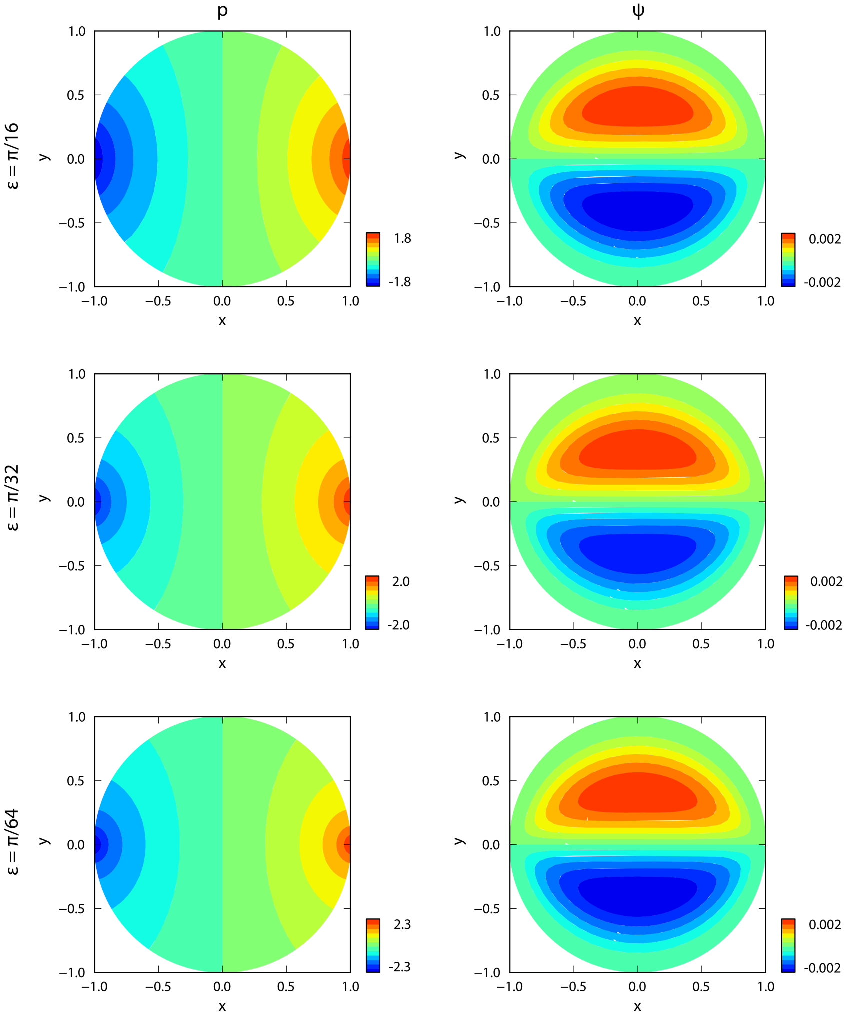

Figure 3.6 Contour plot of pressure and stream function fields at $\lambda = 12.0$. The pressure shows a gradient between the neutral lines, revealing the same asymmetry that drives the circulation through the centre. The pressure gradient is order 1 in this dimensionless solution, corresponding to pressure term of order $P \sim \eta V/R = 10^{-4}$Pa in real units (when substituting $V = 50$ μm/s and $R = 100$ μm. The stream function shows an anti-symmetric maximum and minimum in the upper and lower half planes. The isocontours of these extrema define the advective trajectories fluid elements will follow in the absence of diffusion.

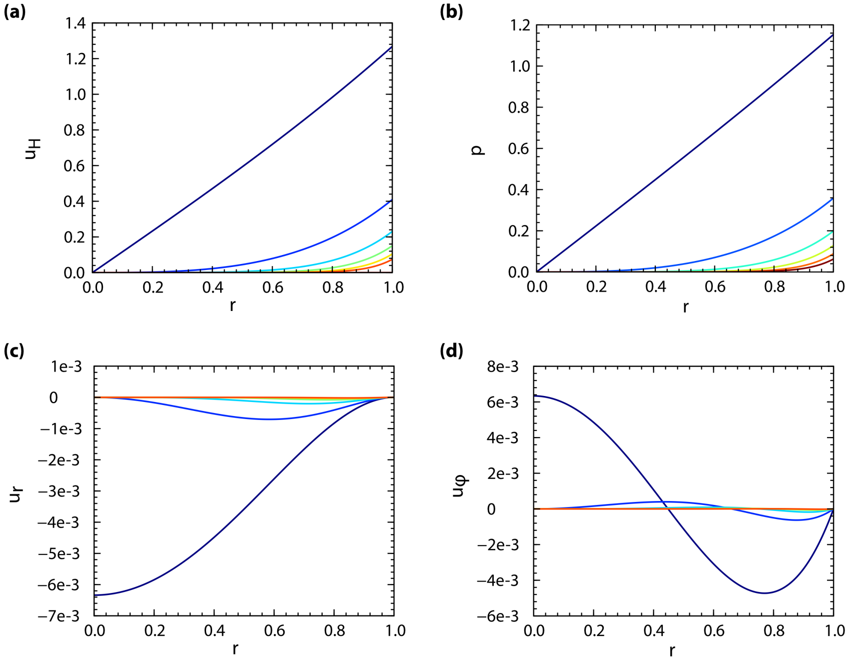

Figure 3.7 Radial modes for vacuolar flow. **(a)** Down-stream modes. **(b)** Pressure modes. (c) Radial modes. (d) Spanwise modes. Note that the circulation in the stream function components result almost entirely from the first-order modes of the expansion, which differ qualitatively from the higher order terms in that they produce a non-zero flow at the centre of the cell.

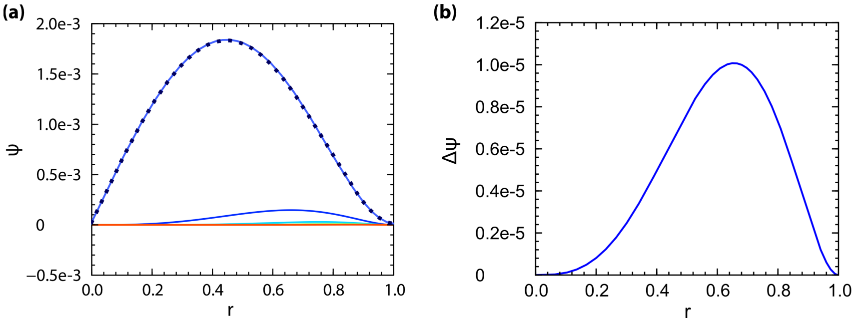

Figure 3.8 **(a)** Modes for the stream function at $\lambda = 12$ and $\varepsilon = \pi/32$. The dotted line shows the empirical approximation $\psi^1(r) \simeq \alpha_\psi r(1-r^2)^2$. **(b)** The deviation of the empirical approximation for the analytical solution $\Delta\psi = \psi^1(r) - \alpha_\psi r(1-r^2)^2$ is of order 0.2% of the mode amplitude a_ψ.

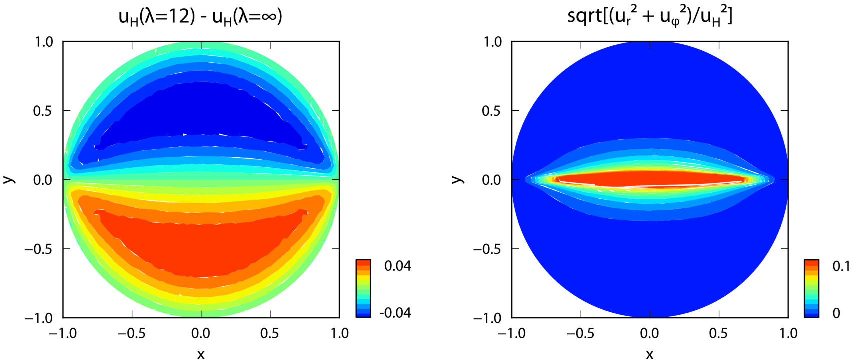

Figure 3.9 Magnitude of the deviation from axial flow at $\lambda = 12$ and $\varepsilon = \pi/32$. **(a)** Difference between downstream component with $\lambda = 12$ and the downstream term of the same solution at $\lambda = \infty$, which is equivalent to Pickard-type axial boundary conditions. **(b)** Magnitude of the stream function components relative to the downstream term.

empirical, it does in fact yield a very close correspondence; at $\lambda = 12$ the relative deviation $|\psi^1(r)/\alpha_\psi - r(1-r^2)^2|$ does not exceed is 0.0016.

To quantify how much the downstream profile of a helical solution deviates from the profile observed in the axial case, we calculate the difference Δw between the downstream profile at $\lambda = 12$ and the downstream profile at $\lambda = \infty$. The result is shown in figure 3.9a. As expected, we see that the solution for the downstream component is in fact very close to the equivalent solution of the axial case (equation 3.8), with deviations not exceeding 4%. Figure 3.9b shows that the deviations arising from the stream function components are most visible along the $y = 0$ centre line where the downstream component approaches zero.

3.2.2 Dependence on the Helical Pitch

Having seen that both the downstream and stream function solutions are qualitatively similar across wavelengths, the dependence of the flow field on the helical pitch is primarily characterised by a change in amplitude of the stream function modes. Figure 3.10 shows the strength of both components as calculated by the root mean square magnitude. The downstream term is shown to be roughly constant across the range of naturally occurring wavelengths, while at shorter wavelengths driving efficiency is reduced as the width of the bands becomes comparable to the cell diam-

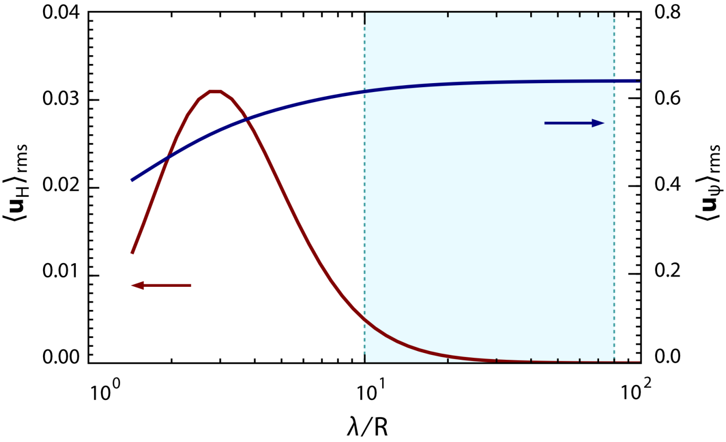

Figure 3.10 Root mean squared magnitude of the two components of flow averaged over the xy-plane. The downstream component (right axis) shows a weak dependence on the helical wavelength. The stream function component is much smaller in magnitude and its amplitude approaches zero for $\lambda \to \infty$ as required by symmetry. For lower wavelengths it attains a maximum at $\lambda = 2.75$ that results from a competition between decreasing driving efficiency and increasing asymmetry as λ approaches zero. The shaded area on the graph indicates the range of wavelengths observed *in vivo*.

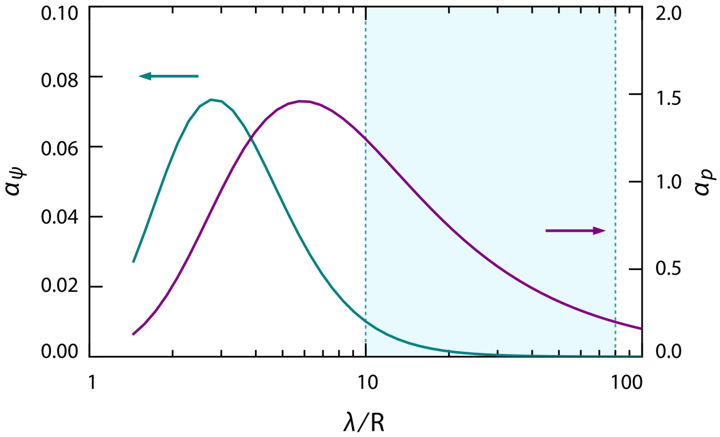

Figure 3.11 Magnitude of helicity as determined by amplitudes of the first modes. (left axis) The stream function amplitude α_ψ (*turquoise*) shows the same basic dependence as the RMS magnitude of the stream function velocity. The maximum of this curve lies at $\lambda = 2.8$ $\alpha_\psi = 0.074$. (right axis) The typical pressure gradient α_p (*magenta*) shows a more extend peak that reaches a maximum of $\alpha_p = 1.5$ at $\lambda = 5.9$.

eter. Note that the mean rate of transport along the z-axis varies more strongly with the wavelength since the projection $\boldsymbol{u}_H \cdot \boldsymbol{e}_z = w/h$ contains an additional factor h. The amplitude of the stream function terms approaches zero at long wavelengths, increasing at shorter wavelengths until a maximum is reached at $\lambda = 2.75$. The magnitude of the stream function component is about 6% of the RMS downstream velocity at the maximum, and should be expected to be about 1% at height of development in a young cell.

The stream function components are dominated by their first mode (fig 3.7), so the amplitude of this mode provides a perhaps more useful measure of the degree of transverse flow. Similarly, the pressure term can be assigned an amplitude in this manner as well. Rather than looking at the extrema of Ψ and p, it proves convenient to use their gradients at $r = 0$ to define two amplitudes:

$$\alpha_\Psi = \partial_r \psi^1(0) = -u_r^1(0) = u_\varphi^1(0) \,, \qquad \alpha_p = \partial_r p^1(0) \,. \tag{3.30}$$

The wavelength dependence of these amplitudes is shown in figure 3.11. The stream function amplitude α_ψ shows a dependence very similar to $\langle \boldsymbol{u}_\Psi \rangle_{\text{rms}}$. The pressure term shows a much broader range of non-axial deviations with a typical magnitude of about 0.1 Pa/m, peaking at a slightly longer wavelength $\lambda = 5.9$.

3.3 Validation with Finite Element Methods

In order to verify that the qualitative form and magnitude of the stream function terms in the solution, we have also obtained solutions for the flow field using a Finite Element Method (FEM) based calculation. The commercially available software package ComSol allows computation of these problems in a relatively straight-forward manner. While resolutions attainable on a full 3-dimensional mesh are limited compared to other methods, this method does provide a robust and well-tested benchmark against which our analytical may be compared.

Figure 3.12 shows the mesh used in our calculations. We simulate the infinite system by using a large-aspect ratio cylindrical mesh of radius 1 and length 24. Application of periodic boundary conditions allows computation of helical solutions whose wavelengths are an integer fraction $\lambda = L/n$ of the length of the mesh. Computations were performed on a single node (Intel T2300 1.66 Ghz CPU, 3 GB RAM) using a mesh con-

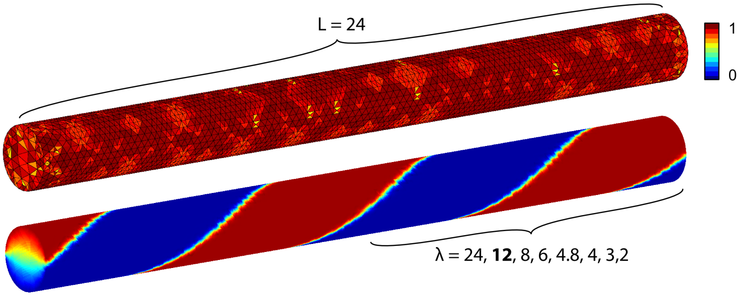

Figure 3.12 (top) Mesh grid used for FEM calculations in ComSol. Colours denote element quality. The mesh used contains 7043 nodes and 29605 elements, which equates to 149876 degrees of freedom (bottom) Boundary values for u_H at $\lambda = 12$. In order to ensure periodicity, solutions are calculated at integer divisions of the longest wavelength $\lambda = 24$.

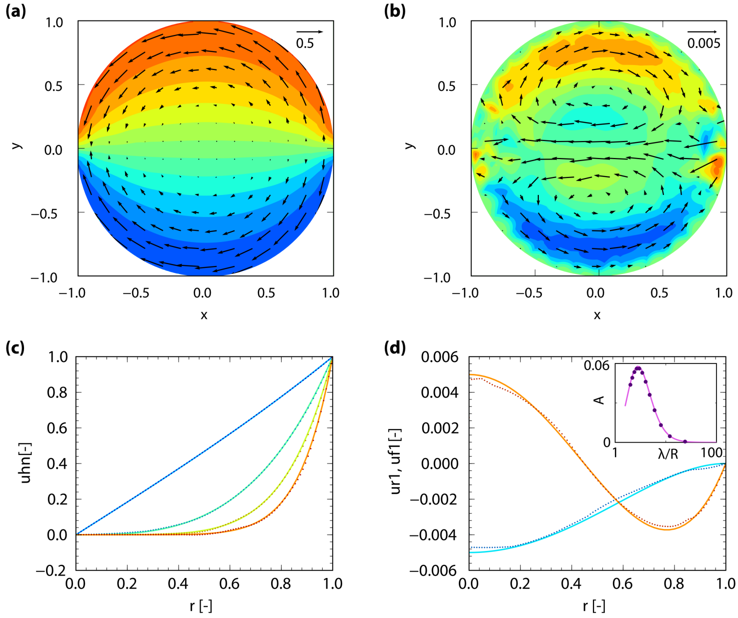

Figure 3.13 Comparison of FEM simulation results with expansion solution at $\lambda = 12$. **(a)** The downstream component u_H, solved for $\varepsilon = \pi/32$. **(b)** The stream function components for the same solution. **(c)** Comparison of the downstream modes for $n = 1, 3, 5, 7$ (dotted) with their analytical equivalents (solid lines). **(d)** Comparison of the (normalized) first modes u_r^1 and u_ϕ^1. (*inset*) Amplitude of the stream function component of the first mode as a function of wavelength (dots) along with the amplitudes obtained from mode-expansion solutions (solid).

taining 7043 nodes and 29605 elements, equivalent to 149876 degrees of freedom in the solved system of equations.

Simulation results are shown in figure 3.13. Both the downstream and stream function components show a highly similar qualitative form to the solutions obtained by mode expansion. A more detailed comparison is shown in the lower panels. In the lower left panel, we show the normalised radial modes as obtained by application of a boundary condition of the form $u_H(1, \varphi) = \sin(n\varphi)$ at $\lambda = 12$. Plotted are slices of the solution at $\varphi = \pi/2$ (dotted) and along with their equivalent solved modes, showing that the two solutions are indistinguishable to simulation precision. The lower right panel shows a comparison of the first modes for u_r (blue) and u_φ (orange) at the same wavelength, showing a good correspondence despite the small magnitude of the terms. In the inset we show the amplitude α_ψ as obtained from the FEM simulations at different wavelengths (dots) along with the mode expansion dependence, showing an near-exact match between the amplitudes.

Summary

So what we've seen in these sections is that the helical form of the flow field in characean internodes is associated with a small transverse circulation that could aid mixing of the vacuolar contents. This circulation is absent in a cell with straight bands, and its magnitude depends strongly on the helical pitch. While the typical amplitudes of non-helically oriented components are two orders of magnitude smaller than the velocity in the bands, the extraordinarily long time scales for diffusion in the system imply that this weak transverse circulation may serve to aid radial redistribution of nutrients, particularly during the phases of growth when the pitch is strongest. The way in which this advection may affect diffusive transport will be discussed further in the next chapter.